Research Article

Influence of Gold Nanoparticle Shape and Single-Cell Localization on Energy Deposition Efficiency and Irradiation Specificity in Photon Radiotherapy

Slobodan Milutinović [ID],[1,2] **Mila Pandurović** [ID],[3] **and Miloš Vujisić** [ID][1]

[1]*University of Belgrade-School of Electrical Engineering, Belgrade, Serbia*
[2]*University of Belgrade-Faculty of Technology and Metallurgy, Belgrade, Serbia*
[3]*"Vinča" Institute of Nuclear Sciences-National Institute of the Republic of Serbia, University of Belgrade, Belgrade, Serbia*

Correspondence should be addressed to Miloš Vujisić; vujsa@etf.rs

Gold nanoparticles (AuNPs) have been investigated extensively in the past twenty years as a sensitizing agent in photon radiotherapy. Targeted delivery of AuNPs to specific sites in cells and tissues contributes to highly localized radiation dose enhancement, whereby the surrounding healthy structures can be largely spared from the unwanted radiation effects. The efficiency of introduced AuNPs with regard to dose enhancement depends on the properties of the nanoparticles since not all of deposited radiation energy reaches the intended biological target but is partially absorbed within the nanoparticles themselves or distributed elsewhere. The present paper investigates the influence of AuNP shape and localization on the enhancement and intracellular distribution of deposited energy in radiation therapy with photons. Energy deposition patterns are calculated with nanoscale accuracy through Monte Carlo simulations of radiation transport, which are optimized to accommodate a structured geometrical representation of the region loaded with AuNPs, i.e., to allow discrete modeling of individual nanoparticles. Same-volume nanoparticles of three commonly encountered shapes—nanospheres, nanorods, and square nanoplates—are examined, in order to inspect the differences in the propagation and absorption of secondary charged particles produced by the incident photons. Five different spatial distributions of spherical AuNPs at the single-cell level are studied in the simulations and compared according to the energy deposited in the cell nucleus. Photon energy, nanoparticle size, and concentration are also varied across simulation runs, and their influence is analyzed in connection to nanoparticle shape and localization. The obtained results reveal how the investigated nanoparticle properties affect their dose-enhancing ability and irradiation specificity in AuNP-augmented radiotherapy.

1. Introduction

Nanoparticles have been studied as radiosensitizers in photon radiotherapy for over two decades now [1–5]. Gold nanoparticles (AuNPs) have attracted special attention for several reasons: they are relatively easily produced in a range of different shapes and sizes, they allow straightforward surface coating and functionalization, and they also have good biocompatibility. When suitably shaped and/or functionalized, AuNPs attain high targeting specificity and can be delivered selectively to cells or subcellular components targeted by photon radiotherapy [6–8]. Due to their high atomic number and density, AuNPs introduced into a specific volume or attached to desired structures can augment local energy deposition via secondary electrons produced in them by the primary photons. By aiming the deposited energy at the chosen targets in this manner, tumor cells or their constituents can be delivered high radiation doses, while at the same time their healthy surroundings can be protected from unwanted radiation effects. This selective dose enhancement depends on nanoparticle properties since not all of deposited radiation energy reaches the intended

biological target but is partially absorbed within the nanoparticles themselves or distributed elsewhere [9–11].

Preclinical studies of nanoparticle-enhanced radiotherapy often rely on Monte Carlo simulations of radiation transport, which can model nanoparticle-laden biological structures, calculate dose distributions within them, and probe the efficacy of various nanoparticles in different irradiation scenarios [12–21]. In the present paper, the influence of gold nanoparticle shape and single-cell localization on the enhancement and intracellular distribution of deposited energy in radiation therapy with photons is investigated through Monte Carlo simulations. To the best of the authors' knowledge, there are only a handful of previous Monte Carlo-based investigations exploring the effects that these nanoparticle characteristics have on the efficacy of radiotherapy augmentation [22–27]. Compared to these research studies, the present study is more detailed with regard to modeling the transport of secondary electrons and more comprehensive with regard to surveyed nanoparticle parameters but also more exact with regard to the central nanoparticle properties being explored. Physical and geometrical models in the simulations have been chosen and adjusted so as to permit discrete representation of individual AuNPs and provide deposited energy distributions with nanoscale precision. The simulation models in the present study differ from those of earlier investigations in that they accentuate the impact of nanoparticle shape and localization on the enhancement of radiotherapy, by defining the geometry of both the AuNPs and of the cell model in a way that is appropriate to this end, as described in Section 2 of the paper. This has allowed the effectiveness of variously shaped or localized AuNPs to be compared independently of other tested influencing factors but still in relation to them. The additional factors that have been changed across simulation runs include the photon energy, nanoparticle size, and concentration, which have all been varied through wider ranges of values than in any of the preceding investigations. The obtained results indicate how the investigated features of AuNPs affect their dose-enhancing capacity and irradiation specificity. Conclusions reached within the study provide guidelines for optimizing the design of AuNPs used for enhancing photon radiotherapy.

2. Methods and Models

Geant4 Monte Carlo toolkit (version 10.7) [28, 29] was used for performing numerical experiments within the present study. Simulations of particle transport were executed on a computer with an AMD Ryzen™ Threadripper™ 1950X Processor [30] and 32 GB RAM memory. Nanoscale distributions of deposited energy were obtained by utilizing the Livermore condensed history algorithm for electron transport in Geant4, with parameters of the algorithm adjusted so as to bring it as close as possible to true event-by-event particle tracking (see Appendix A). The level of detail provided by this physical model allows the nanoparticle-laden volume to be modeled as a structured region, with NPs represented as discrete geometrical entities distributed within it, and enables nanodosimetric calculations to be

carried out [31]. Physical models chosen for and attuned to nanoscale precision of dose calculations are too complex and demanding for macroscopic calculations and preclude large-scale simulations (such as those at tissue level) from being conducted within any reasonable time frame, even with optimized computer resources. The so-called mixture approach, on the other hand, treats the nanoparticle-loaded region as a homogeneous metal-tissue blend and requires a less detailed representation of electron transport, thereby permitting larger radiotherapy target regions to be handled by the simulations, but can yield only *macroscopic* dosimetric quantities as the output [32–34]. Results of simulations carried out for the present paper supplement the information provided by the mixture approach, by relying on nanodosimetric calculations and analyzing how shape and localization of AuNPs affect the distribution of deposited energy.

Instead of modeling a macroscale target volume, a smaller *representative volume* was introduced, which exemplified the region loaded with AuNPs. A single such volume, containing one or more NPs, constituted the geometrical model used in simulations. Any nanoparticle-laden region can be thought of as comprising a multitude of identical representative volumes, stacked with no overlaps or gaps. The representative volume was cubic in all simulations but differed in size and content in parts of the investigation concerned with shape and localization of NPs.

It was assumed in the simulations that electronic equilibrium existed in the representative volume, since in a larger nanoparticle-laden region it would have been surrounded by other such volumes exposed to the same photon field. The assumption of electronic equilibrium was justified even for inhomogeneous nanoparticle localizations within the representative volume (described in Section 2.2), since all adjacent volumes would contain the same inhomogeneities in AuNP distribution as the volume observed in simulations. Modeling of the electronic equilibrium, i.e., of the state in which for each electron leaving the representative volume there is another such electron entering it from the surrounding tissue, was accomplished by modifying the Geant4 source code so that all electrons impinging on the boundary surface of the representative volume from the inside were specularly reflected back into the volume.

2.1. Nanoparticle Shape. In simulations probing the influence of nanoparticle shape, the representative volume was a water-filled cube (water serving as a tissue substitute, categorized as material G4_Water in Geant4) containing a single gold nanoparticle (material G4_Au in Geant4) (Figure 1). For each specified size of the nanoparticle and each specified nanoparticle concentration, the volume of the cube was determined as

$$V_{\text{cube}} = V_{\text{NP}} + V_W = V_{\text{NP}}\left(1 + \frac{\rho_{\text{Au}}}{k\rho_W}\right), \tag{1}$$

where ρ_{Au} and ρ_W are the mass densities of gold and water, and the volume of water filling the cube was expressed as $V_W = m_W/\rho_W = m_{\text{Au}}/(k\rho_W) = V_{\text{NP}}\rho_{\text{Au}}/(k\rho_W)$ so that it
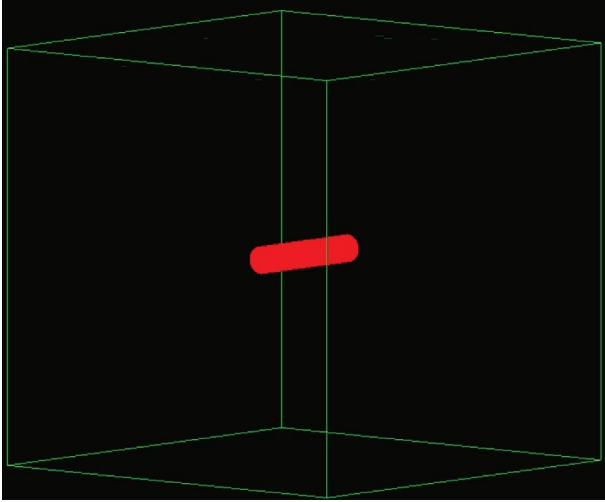
FIGURE 1: A single gold nanorod at the center of the water-filled cubic representative volume. In simulations probing the influence of nanoparticle shape, the representative volume contained only a single nanoparticle—either a nanosphere, a nanorod, or a nanoplate—in each simulation run. The size of the representative volume was varied so as to reflect different nanoparticle concentrations.

corresponded to the set value of nanoparticle mass concentration $k = m_{Au}/m_W$ (expressed as milligrams of gold per gram of water, i.e., (mg Au)/(g H_2O)). For AuNPs of different sizes and concentrations investigated herein, the edge of the cube, obtained from equation (1), ranged between 79.70 nm and 2.163 μm.

Three commonly produced shapes of AuNPs were inspected—nanospheres, nanorods, and square nanoplates (Figure 2)—and compared according to the energy deposited in the surrounding medium (i.e., water in the cube). Only this energy, which does not get absorbed inside the nanoparticles themselves, can potentially contribute to damaging targeted cellular moieties. Simulation results were compared for same-volume nanoparticles of the three investigated shapes. Three different nanoparticle sizes were used. The diameter of the nanosphere was set at $d = 10$, 50, or 100 nm. Dimensions of cylindrical nanorods and square nanoplates were then calculated for each of these three cases so that all three shapes had the same volume. The ratio of dimensions was set arbitrarily at D : H = diameter : height = 1 : 5 for nanorods, and at $a : b : c = 1 : 100 : 100$ for nanoplates. With an adopted nanosphere diameter d, the matching dimensions of the other two nanoparticle shapes were then found as

$$D = \frac{d}{\sqrt[3]{7.5}}, \ H = 5D,$$

$$a = d \sqrt[3]{\frac{\pi}{60000}}, \ b = c = 100a. \tag{2}$$

For the three investigated sizes, the volume of the nanoparticle was 523.6 nm^3, 65450 nm^3, and 523600 nm^3.

At any particular moment during external beam photon radiotherapy, a region loaded with gold nanorods or nanoplates is exposed to a unidirectional photon beam

and the nanoparticles assume various orientations with regard to the direction of the beam. Assuming no specific attachment of the NPs occurs at the subcellular level, there is a uniform distribution of nanorods or nanoplates inside the region with regard to both position and orientation. To represent nanorods or nanoplates distributed uniformly across all possible orientations in space, the orientation of the single nanoparticle contained by the cubic representative volume would have to be sampled anew for each photon from a unidirectional beam incident on the cube. Rather than simulating a unidirectional beam and changing the orientation of the nanoparticle for each incoming photon, the nanoparticle was positioned at the center of the cubic representative volume and fixed in an arbitrarily chosen orientation. The cube with the nanoparticle was then exposed to an isotropic field of photons, incident on the cube from all possible directions.

Simulation outputs were the energies deposited in the nanoparticle E_{np} and in the surrounding water E_w. Fraction of deposited energy which went into water was then found as

$$\delta_w^i = \frac{E_w^i}{E_w^i + E_{np}^i}, \tag{3}$$

where the superscript i distinguishes between the three investigated nanoparticle shapes ($i = sphere$, rod, or $plate$). Since water acted as a substitute for tissue in the simulations, only the energy deposited in water was considered exploitable from the perspective of any radiotherapeutic and biological effect. In view of this, equation (4) expresses the *usable fraction of deposited energy*. The influence of nanoparticle shape was quantitatively expressed by the relative usable fraction of deposited energy with respect to spherical AuNPs:

$$\Delta^i = \frac{\delta_w^i - \delta_w^{sphere}}{\delta_w^{sphere}}, \quad i = rod, plate. \tag{4}$$

2.2. Nanoparticle Localization. In simulations probing the influence of the localization of nanoparticles within a single cell, the representative volume was a cube with a sphere centered within it. Dimensions of both the cube and the sphere were fixed in all simulation runs: the edge of the cube was set at 15.04 μm, while the sphere's diameter was 4.329 μm. This representative volume was adopted as a simple model of a mammalian cell, with a spherical nucleus inside the cytoplasm. More specifically, hepatocyte cells served as a basis for such a model, in both shape and dimensions. The whole of the cube, including the sphere at its center, was filled with water (G4_Water in Geant4). The nucleoplasm and the cytoplasm have thus been modeled as being composed of liquid water of the same density, even though their mass densities actually differ and vary across cell types [35, 36]. Such a choice for the cell model allowed the influence of nanoparticle localization to be investigated
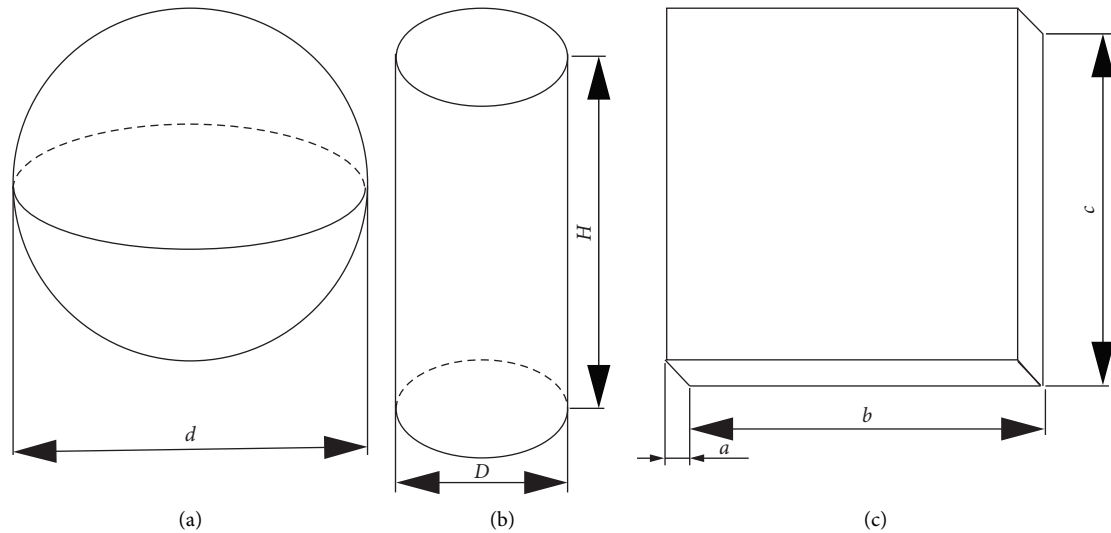
FIGURE 2: Illustration of three investigated AuNP shapes: (a) nanosphere, (b) nanorod, and (c) square nanoplate. The illustrations are not to scale—nanoparticle dimensions are stated in the text.

independently of these variations and also the results to be compared to those from previous studies dealing with nanoparticle-enhanced radiotherapy, many of which adopted the same approximation [22, 24, 25].

Different localizations of AuNPs at the single-cell level were compared according to energies deposited in the nanoparticles and delivered to the cell nucleus (i.e., to the sphere at the center). Nucleus was chosen as the targeted subunit under the commonly adopted assumption that it is the most radiation sensitive part of the cell, being the central regulator of cell metabolism and cell cycle management [37, 38].

Gold nanospheres were localized in the representative volume in five different ways:

(i) Only inside the central sphere (i.e., inside the nucleus, Figure 3(a)).

(ii) At the sphere's outer surface (i.e., attached to the nuclear envelope, Figure 3(b)).

(iii) Everywhere inside the cube except in the sphere (i.e., around the nucleus, Figure 3(c)).

(iv) At the cube's inner surface (i.e., attached to the cell membrane).

(v) Everywhere inside the cube, including the sphere (the case of no subcellular localization).

The diameter of nanospheres took three different values in various simulation runs: $d = 10$, 50, or 100 nm. These are the same three diameters used for the single nanosphere in simulations probing the influence of nanoparticle shape, described in Section 2.1. For various concentrations and sizes of the AuNPs, their number ranged from 336 to 6 719 213.

In all five investigated cases of localization, positions of AuNPs were sampled uniformly within the region or at the surface of localization. Efficient algorithms were needed for sampling the positions of AuNPs, especially in conditions when their number was high.

For distributing the nanospheres inside the cubic representative volume or inside its central sphere, the cube or the sphere was first voxelized, i.e., partitioned into identical cubic volume elements. Smallest possible voxels were used, which meant that in almost all simulation runs the edge of the voxel was made equal to the nanosphere diameter d or slightly larger to provide exact partitioning of the cube. Only in two cases which turned out especially demanding with regard to computer RAM capacity—those of 10 nm nanospheres either distributed around the central sphere or having no subcellular localization—did the voxel have to be made considerably larger than the nanosphere, and its edge was set to 20 nm. For each nanoparticle that needed to be placed, a voxel was then chosen uniformly from the collection of voxels constituting the region of localization. The random selection of voxels was confined to the region of localization—the central sphere, the part of the cube surrounding this sphere, or the whole of the cube's inner volume. The nanosphere being sited was then positioned at the center of the chosen voxel.

The same method was applied to distributing the nanospheres uniformly at the inner surface of the cubic representative volume, except that only the layer next to the cube's surface was voxelized.

The number of AuNPs that needed to be distributed uniformly within this layer was never greater than the number of voxels, so a single layer of voxels was sufficient in all cases.

For distributing the nanospheres uniformly at the outer surface of the central sphere, the regular placement algorithm described in [39] was utilized. The size of the nanospheres set for any current simulation run determined the number of possible nanoparticle sites, i.e., equidistributed points at the surface of the sphere that could become centers of nanospheres if chosen by uniform sampling. The said algorithm provided these possible sites, from which the positions for the nanospheres were then chosen uniformly. In cases when the number of AuNPs was greater than the
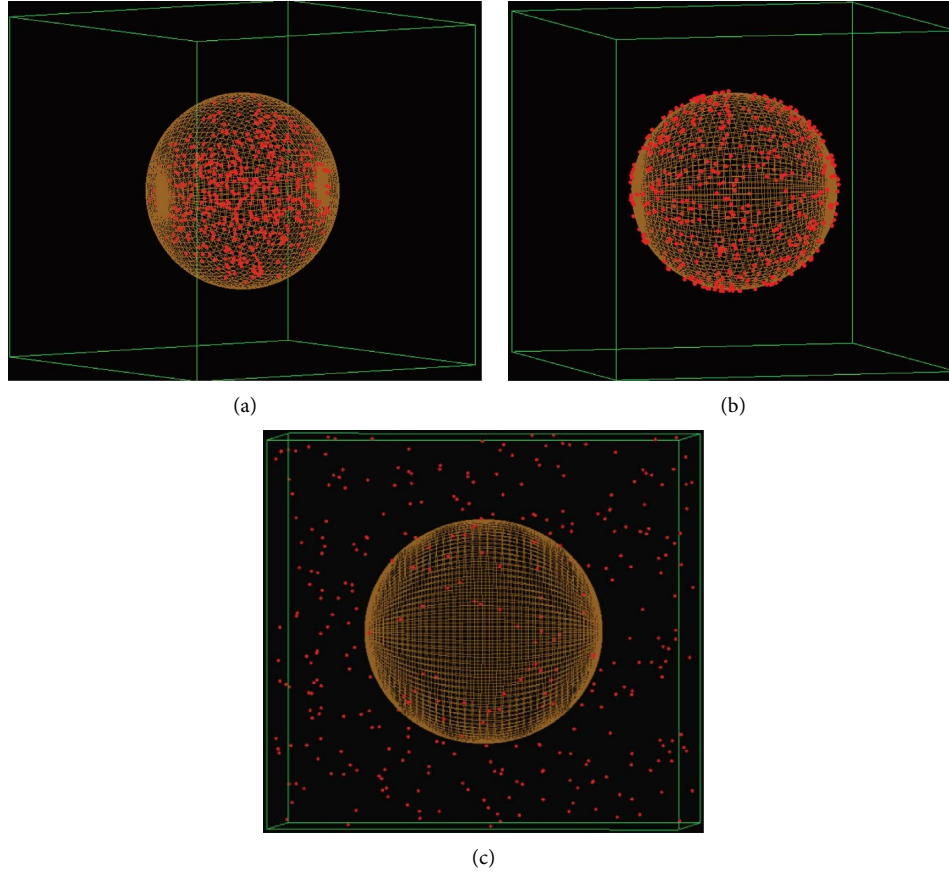
(a)

(b)

(c)

FIGURE 3: Illustration of three (out of the five investigated) subcellular AuNP localizations: (a) inside the central sphere, (b) at the sphere's outer surface, and (c) around the sphere. The two remaining cases (with NPs attached to the cube's inner surface and the other with no localization) were not suitable for clear graphical representation.

number of possible sites at the surface, the sites were all filled by nanospheres, and another layer of sites was found above the first one for distributing the rest of NPs. Depending on the total number of NPs that needed to be placed, spherically curved layers of such possible sites were stacked one on top of another until all NPs were placed. In this way, all but the top-most layer were completely filled, and the top layer contained NPs distributed uniformly.

A parallel monoenergetic photon beam was incident perpendicularly on one face of the cubic representative volume. The beam had a square cross section, equal to the representative volume's face.

Simulation outputs were the energies deposited in the nanoparticles E_{np}, the nucleus $E_{nucleus}$ (i.e., the central sphere), and the extranuclear part of the cell E_{cyto} (i.e., the cytoplasm outside the central sphere). Fractions of deposited energy which went into the nucleus and into the nanoparticles were then calculated as

$$\delta_{nucleus}^{i} = \frac{E_{nucleus}^{i}}{E_{np}^{i} + E_{nucleus}^{i} + E_{cyto}^{i}},$$

$$\delta_{np}^{i} = \frac{E_{np}^{i}}{E_{np}^{i} + E_{nucleus}^{i} + E_{cyto}^{i}},$$

(5)

where the superscript i distinguishes between the five investigated nanoparticle localizations. Different nanoparticle localizations were compared with regard to these two fractions.

2.3. General Simulation Parameters. The energy of the isotropic photon field in simulations examining the influence of nanoparticle shape, as well as of the parallel photon beam in simulations inspecting the influence of nanoparticle localization, ranged from 20 keV to 4 MeV, with the following energies from this range used in various simulation runs: 20, 30, 50, 80, 81, 150, and 500 keV, as well as 4 MeV.

Three different concentrations of AuNPs were specified for each of the cases pertaining to various nanoparticle shapes, localizations, and sizes: $k = 1$, 7, and 20 (mg Au)/(g H_2O). As previously explained, in simulations examining nanoparticle shape, the change in nanoparticle concentration required the size of the cubic representative volume to be changed accordingly, as seen from equation (1), since this volume contained only a single NP. In simulations examining nanoparticle localization, on the other hand, the size of the representative volume was fixed, and the change in nanoparticle concentration affected the number of AuNPs that needed to be distributed in the current simulation run.

TABLE 1: Properties of gold nanoparticles used in simulations probing the influence of nanoparticle shape.

Nanoparticle shape	Linear dimensions (nm)	Volume (nm^3)	V/S (nm)	Mean straight-line path (nm)
Sphere	d: 10.00		1.667	3.749
Nanorod	D, H: 5.109, 25.54	523.6	1.161	2.952
Nanoplate	a, b, c: 0.3741, 37.41, 37.41		0.1834	0.9355
Sphere	d: 50.00		8.333	18.75
Nanorod	D, H: 25.54, 127.7	65450	5.805	14.76
Nanoplate	a, b, c: 1.871, 187.1, 187.1		0.9170	4.678
Sphere	d: 100.0		16.67	37.49
Nanorod	D, H: 51.09, 255.4	523600	11.61	29.52
Nanoplate	a, b, c: 3.741, 374.1, 374.1		1.834	9.354

The number of photon histories was chosen independently for each simulation run, so as to ensure that the relative uncertainty of deposited energy values calculated from simulations was under 1%.

This was achieved in 97% of simulation runs. In the remaining cases (17 out of 576 runs), the uncertainty ranged between 1.3 and 2.5%, exceeding 2% only for smallest nanoparticles at a concentration of 1 (mg Au)/(g H$_2$O) exposed to 150 keV photons (a total of 3 cases encountered in simulations probing the influence of nanoparticle shape). With all that said, the number of photon histories ranged from 10^7 to $1.4 \cdot 10^{11}$ in various runs.

3. Results and Discussion

Previous investigations of gold nanoparticle-enhanced photon radiotherapy have shown that, if nanoparticle concentration and the energy of incident photon beam are both kept constant, absorbed dose in tissue decreases with increasing nanoparticle size. The decrease is caused by the absorption of secondary electrons in the nanoparticles themselves, an effect referred to as *self-absorption*. The increase of nanoparticle concentration in tissue, on the other hand, increases the dose deposited in it, with other parameters kept constant [10, 13, 31, 34]. However, this increase is limited by another absorption effect, referred to in our previous investigation as *crossfire*, in which secondary electrons emitted by a nanoparticle can get absorbed by its neighbouring NPs—a phenomenon that becomes more prominent as the concentration of nanoparticles rises. A third pathway by which radiation energy can be lost to nanoparticles is termed *influx* and pertains to secondary electrons that originate in the tissue but get absorbed in the NPs.

In the following, results of simulations and calculations described in Section 2 are presented and discussed separately for effects observed with differently shaped and variously localized nanoparticles.

3.1. Influence of Nanoparticle Shape. Geometrical properties of gold nanoparticles with the three investigated shapes and of three different sizes are summarized in Table 1. In addition to the dimensions stated in Section 2.1, this table states two more nanoparticle characteristics: their volume-to-

surface ratio (V/S) and their mean straight-line path. The latter quantity is the mean distance between the position at which an electron is produced within a nanoparticle by an incident photon and the point at which that electron would exit the nanoparticle, if it were moving along a straight line. Such a trajectory would only be possible if the electron did not undergo any interaction along the path inside the nanoparticle. However, for most electron energies investigated in this study, the inelastic mean free path of electrons in gold is on the same order as the nanoparticle dimensions or less [40–42]. Therefore, the mean straight-line path can serve only as a first-order approximation of the mean path length that electrons need to travel within a nanoparticle in order to exit it. Nevertheless, it presents a useful means for interpreting the results on the partition of the deposited radiation energy provided by the simulations. It is a purely geometrical property of a particularly shaped nanoparticle that offers straightforward insight into the mean energy which the electrons can carry out of it. The mean straight-line path was calculated for all examined AuNP shapes and sizes in a separate set of Monte Carlo simulations, by sampling isotropic directions from points which were themselves sampled uniformly within the nanoparticle.

Graphs in Figure 4 show how the relative usable fraction of deposited energy with respect to spherical AuNPs (Δ^i, $i = rod$, $plate$) depends on the photon beam energy. Values of Δ^i were calculated from equation (5), based on simulation outputs inserted into equation (4). Figures 4(a)–4(c) correspond to nanoparticle concentrations of 1, 7, and 20 (mg Au)/(g H$_2$O), respectively.

The dependence of Δ^i on photon beam energy is shown again in Figure 5, but with each subfigure corresponding to a different nanoparticle size, defined by the diameter of the nanosphere: $d = 10$, 50, and 100 nm for Figures 4(a)–4(c), respectively.

Graphs in Figures 4 and 5 demonstrate that there is a noticeable influence of nanoparticle shape on the usable fraction of deposited radiation energy. This can be attributed to the geometrical argument: the mean path length that has to be traversed by a secondary electron in order to escape the nanoparticle is different for various nanoparticle shapes, as Table 1 indicates, being largest for the nanosphere and shortest for the nanoplate. Since the number of electron interactions with the Au atoms rises with the electron path
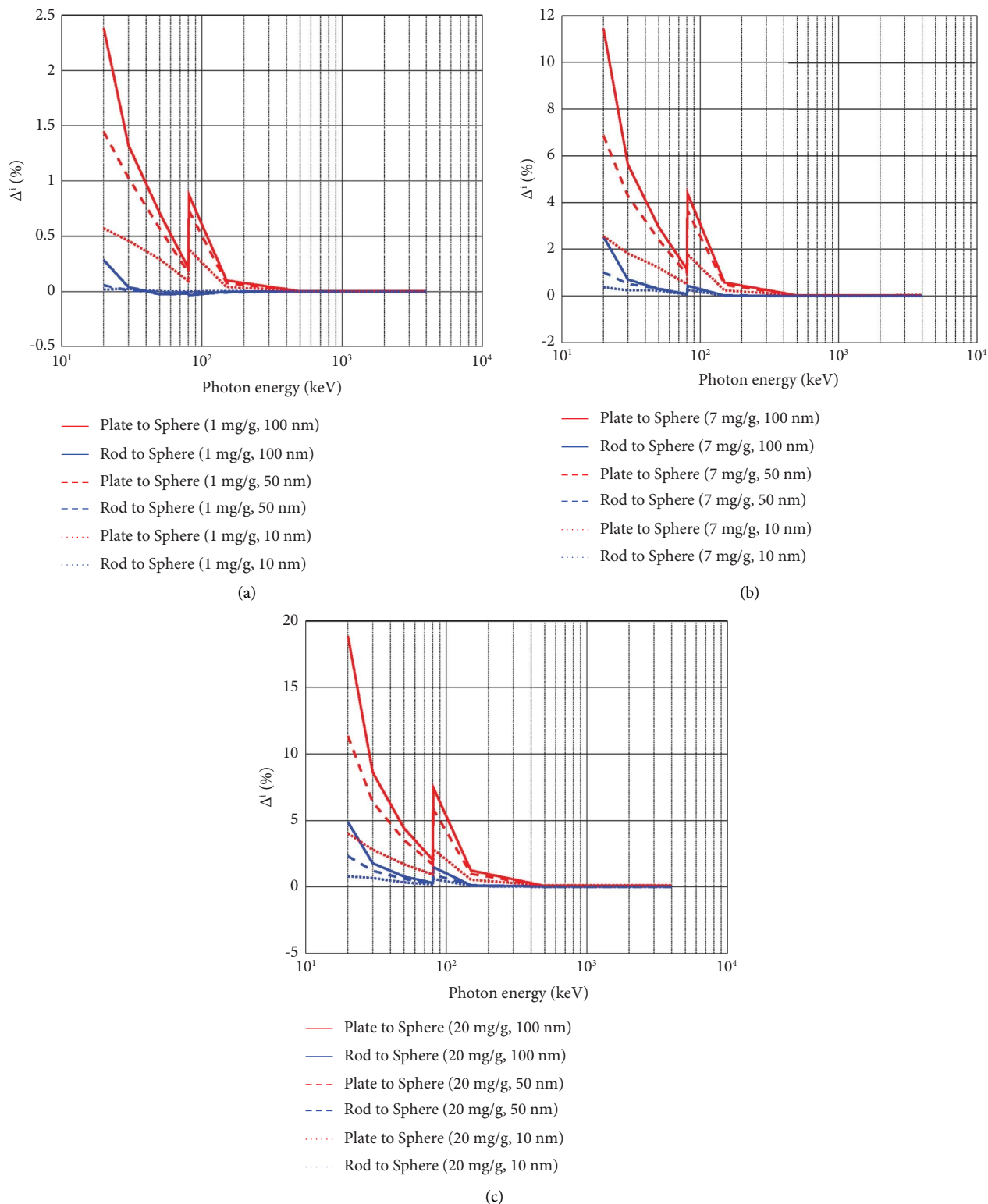
(a)

(b)

(c)

FIGURE 4: Influence of AuNP shape. Graphs show the dependence of the relative usable fraction of deposited energy with respect to spherical AuNPs Δ^i ($i = rod$, $plate$) on the photon beam energy for nanoparticle concentrations of (a) 1 (mg Au)/(g H_2O), (b) 7 (mg Au)/(g H_2O), and (c) 20 (mg Au)/(g H_2O). At each concentration, red graphs pertain to gold nanoplates and blue graphs to gold nanorods, while different lines of the same color (solid, dashed, and dotted) refer to three diameters of gold nanospheres (100, 50, and 10 nm, respectively). Nanorods and nanoplates were of the same volume as the nanospheres.
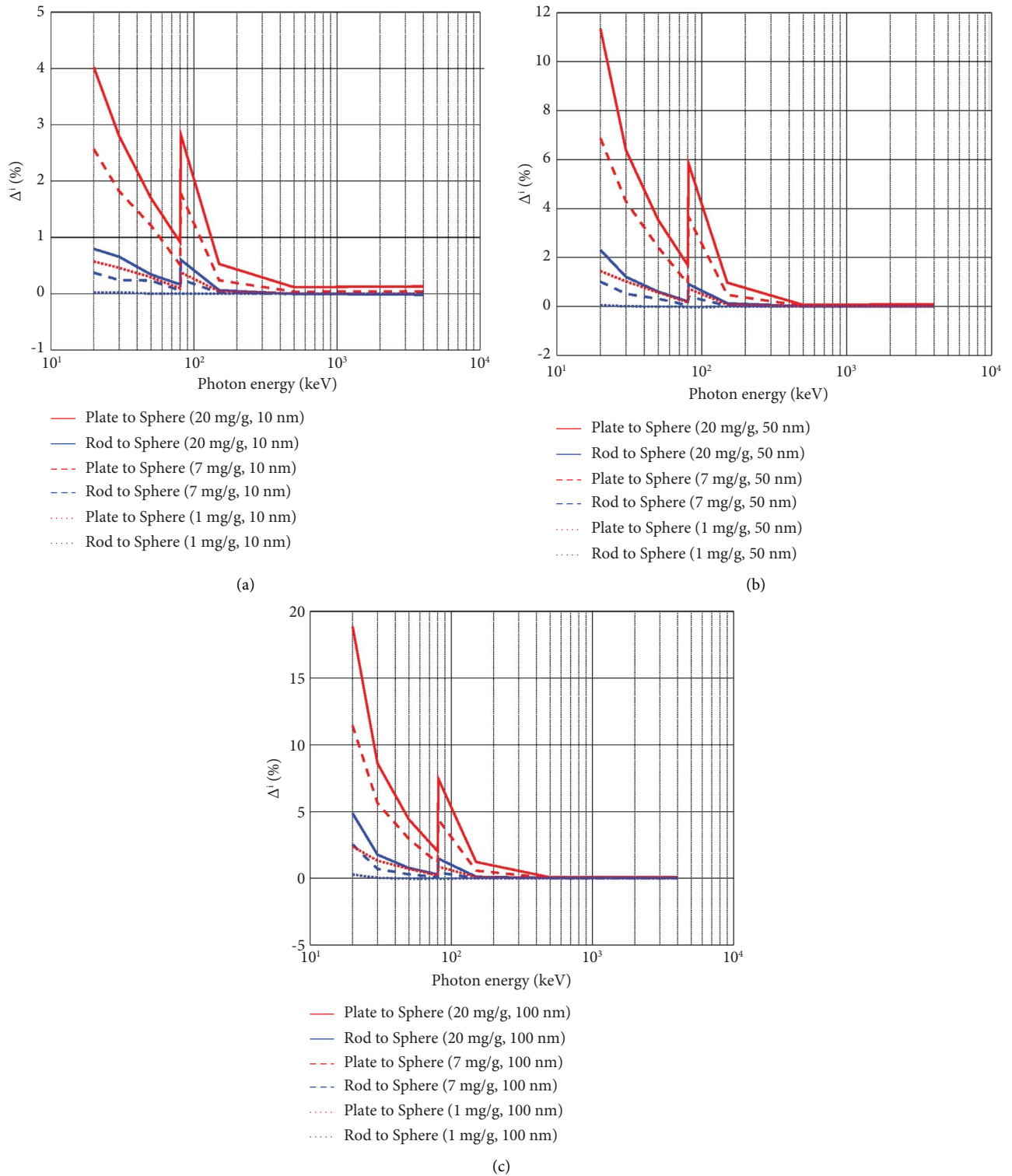
(a)

(b)

(c)

Figure 5: Influence of AuNP shape. Graphs show the dependence of the relative usable fraction of deposited energy with respect to spherical AuNPs Δ^i ($i = rod, plate$) on the photon beam energy for the nanosphere diameter of (a) 10 nm, (b) 50 nm, and (c) 100 nm. Nanorods and nanoplates were of the same volume as the nanospheres. For each nanoparticle size, red graphs pertain to gold nanoplates and blue graphs to gold nanorods, while different lines of the same color (solid, dashed, and dotted) refer to three nanoparticle concentrations (20, 7, and 1 (mg Au)/(g H$_2$O), respectively.

length, it consequently leads to an increase in self-absorption within the AuNP. This implies that in the case of spherical AuNPs, the probability for self-absorption is higher compared to the other two investigated shapes. In agreement with this, Figures 4 and 5 show that the usable fraction of deposited energy is highest for the nanoplate and lowest for the nanosphere. This means that, out of the three investigated nanoparticle shapes, plate is the most favorable from the dosimetric point of view, while sphere is the least favorable.

Figure 4 shows that the value of Δ^i increases with the rise of AuNP size, for both rod and plate nanoparticles. Moreover, the difference between Δ^{plate} and Δ^{rod} is increasing with the rise of AuNP size. So, the influence of nanoparticle shape on the usable fraction of deposited energy, and consequently on the absorbed dose received by tissue, becomes more prominent with increasing nanoparticle size. The same trend is observed for increasing nanoparticle concentration, for all three examined AuNP shapes (Figure 5).

Figures 4 and 5 also demonstrate that the influence of nanoparticle shape on the usable fraction of deposited energy is different for different irradiation conditions. At lower photon beam energies, nanoparticle shape can contribute observably to the usable fraction of deposited energy, while at higher energies, this influence becomes negligible. The most prominent example is observed at the photon energy of 20 keV for AuNPs with largest size and highest concentration. The usable fraction of deposited energy in this case is 19% higher for nanoplates than for nanospheres. A general observation is that Δ^i declines with the rise of photon energy, except at the K-edge of gold (at 80.7 keV).

The observation that the influence of nanoparticle shape on radiation energy delivered to tissue is negligible at high photon beam energies is a valuable result in itself, since the computer processing time needed for a simulation at a photon energy above 100 keV can be up to two orders of magnitude longer than at lower energies. Having this in mind, future investigations of the impact of nanoparticle shape can be limited to low photon energies (<100 keV), which are less demanding of computational resources.

3.2. Influence of Nanoparticle Localization. The fraction of deposited energy which went into the nucleus $\delta^i_{nucleus}$ was calculated for all five investigated intracellular nanoparticle localizations by inserting simulation outputs into equation (5). The results are presented in Figures 6 and 7. In Figure 6, each subfigure corresponds to a different nanoparticle concentration (namely, Figures 6(a)–6(c) correspond to nanoparticle concentrations of 1, 7, and 20 (mg Au)/(g H_2O), respectively). The same results are presented in Figure 7 but with each subfigure corresponding to a different nanoparticle size (with Figures 7(a)–7(c) corresponding to nanoparticles with a diameter of 10, 50, and 100 nm, respectively).

These results show that the choice of nanoparticle localization has a significant impact on the energy deposited within the nucleus. As expected, $\delta^i_{nucleus}$ decreases with the

distance of AuNPs from the nucleus. The nucleus receives the highest fraction of deposited energy when AuNPs are inside it and second-highest when AuNPs are attached to the nuclear envelope. These two cases can be termed "near" localizations. They are followed by the case of no subcellular localization. The two "far" localizations come last according to $\delta^i_{nucleus}$: the case when AuNPs are distributed around the nucleus and finally the case when AuNPs are attached to the cell membrane. In comparison to the case of no localization, the energy delivered to the nucleus can be several times higher for "near" localizations (up to 5.475 times), or up to 2.345 times lower for "far" localizations. For two extreme localizations (AuNPs localized inside the nucleus and attached to the cell membrane), the fraction of deposited energy that goes into the nucleus can differ up to 12.84 times.

The impact of localization on the energy delivered to the nucleus shows different behaviors for low- and high-energy photons, as can be seen in Figures 6 and 7. In the low-energy region, the influence of localization is highly pronounced. However, this influence generally lessens with the increase of photon beam energy, becoming irrelevant at beam energies above 150 keV. In the following, a discussion of the behavior of δ^i for various nanoparticle localizations in the low-energy region is presented.

Opposite trends are observed in the dependence of $\delta^i_{nucleus}$ on photon beam energy for "near" and "far" localizations. For "near" localizations, $\delta^i_{nucleus}$ depends strongly on the energy of the incoming beam and decreases as the photon beam energy increases. On the other hand, for "far" localizations, $\delta^i_{nucleus}$ does not exhibit such a strong dependence on the energy of the incoming beam, and it increases with the rise of photon beam energy. These opposite trends can be explained by the behavior of secondary electrons produced in photon interactions with AuNPs. For the "near" localizations, high-energy secondary electrons are more likely to carry a large part of their energy away from the nucleus and into the cytoplasm. Conversely, for "far" localizations, the rise of energy increases the probability of secondary electrons reaching the nucleus. In the case of no localization, $\delta^i_{nucleus}$ is almost independent of the incident beam energy throughout the investigated energy range.

The decreasing/increasing trends of the fraction of deposited energy which went into the nucleus have a discontinuity at the energy of the K-edge of gold, i.e., at 80.7 keV. The magnitude of the K-edge jump depends on the investigated parameters. It is most prominent for intranuclear localization, low AuNP diameters, and high nanoparticle concentrations. The direction of the K-edge discontinuity differs for "near" and "far" nanoparticle localizations, with δ^i experiencing an upward jump at this energy for "near" and a downward jump for "far" localizations. Consideration of secondary electrons again accounts for this difference. At a photon energy just above the K-edge, the abrupt rise in photoabsorption probability leads to an increased production of secondary electrons with an energy equal to the small difference between the energy of the absorbed photon and the K-shell binding energy (i.e., the K-edge energy) of gold. Such low-energy K-shell photoelectrons, which then manage to exit the
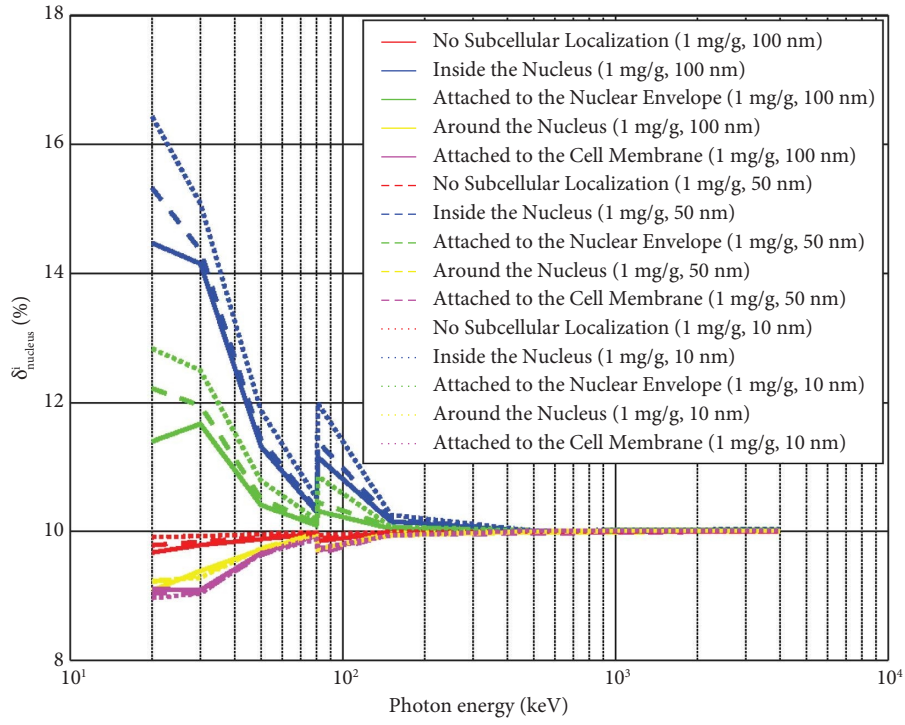
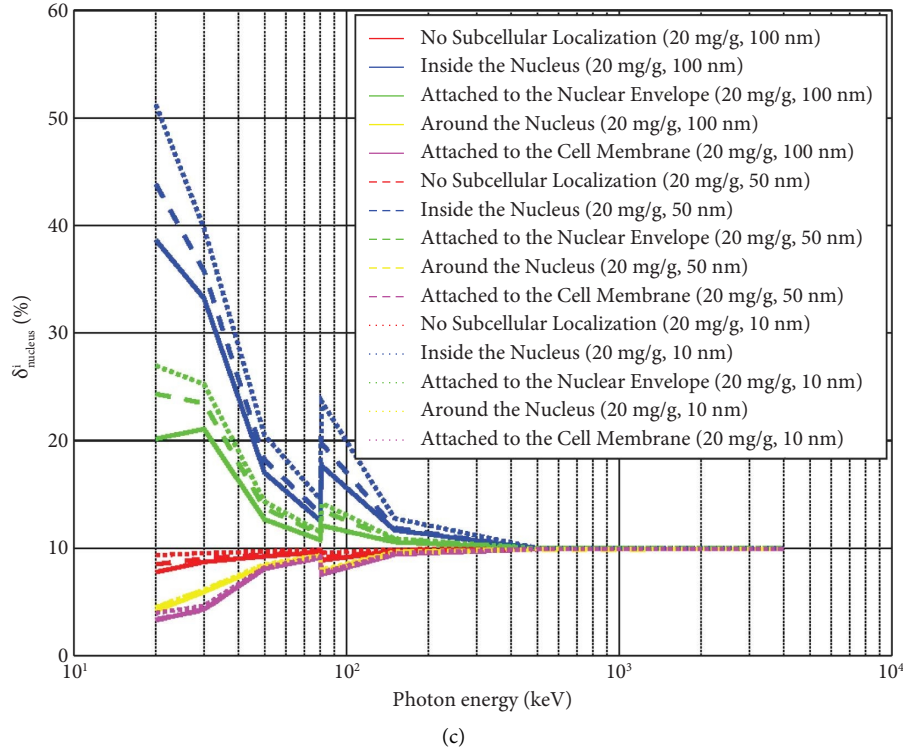(a)
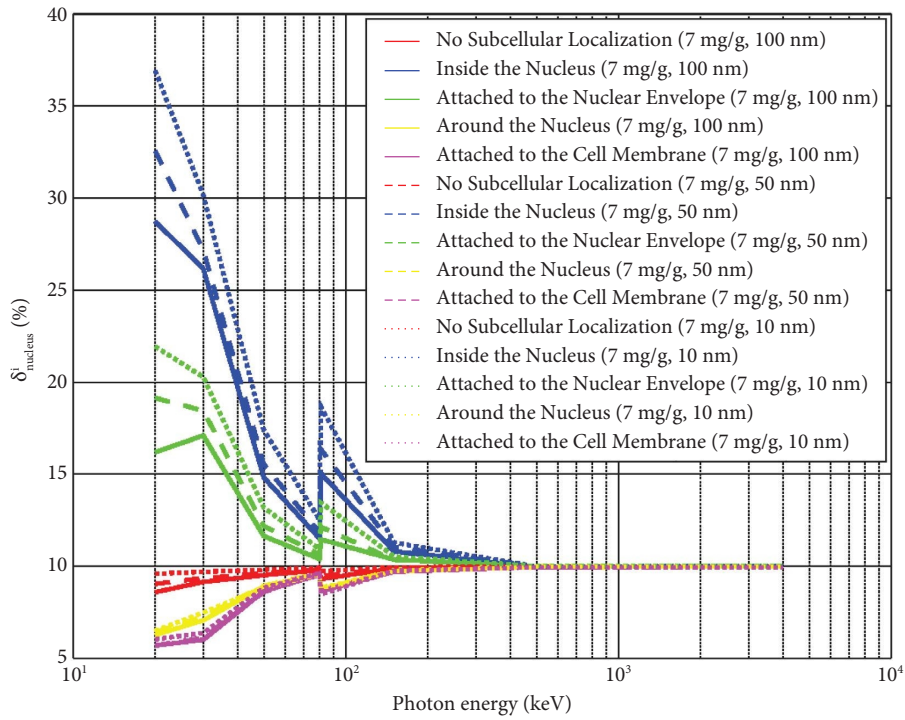
(b)

FIGURE 6: Continued.

(c)

FIGURE 6: Influence of spherical AuNP intracellular localization. Graphs show the dependence of the fraction of deposited energy delivered to the nucleus $\delta^i_{nucleus}$ on the photon beam energy for nanoparticle concentrations of (a) 1 (mg Au)/(g H$_2$O), (b) 7 (mg Au)/(g H$_2$O), and (c) 20 (mg Au)/(g H$_2$O). At each concentration, graphs of various colors pertain to the five different nanoparticle localizations, while different lines of the same color (solid, dashed, and dotted) refer to three nanoparticle diameters (100, 50, and 10 nm, respectively).

AuNPs, have short ranges and are stopped near the nanoparticles from which they originate. This amounts to a higher fraction of deposited energy going to the nucleus in cases of "near" nanoparticle localizations and lower $\delta^i_{nucleus}$ nucleus in cases of "far" localizations. With further increase of photon energy, K-shell photoelectrons' ranges also increase and they deposit ever larger portions of their energies away from the AuNPs, resulting in δ^i curves assuming the same trends as below the K-edge energy.

Figure 7 shows that for "near" localizations and examined concentrations, $\delta^i_{nucleus}$ rises with nanoparticle concentration. However, for "far" localizations, an opposite behavior is again observed. Therefore, nanoparticle localization becomes more significant with the rise of their concentration.

For 100 nm diameter AuNPs attached to the nuclear envelope (solid green curves in Figure 6 and all three green curves in Figure 7(a)), a slight deviation from the general decreasing trend of $\delta^i_{nucleus}$ curves is observed at low photon energies. The rise of $\delta^i_{nucleus}$ as photon energy increases from 20 to 30 keV in this case may come from the range of a secondary electron becoming large enough for it to both escape from the NP in which it originated and traverse one whole neighbouring NP before depositing the rest of its energy in the nucleus. Such a rise is not observed in $\delta^i_{nucleus}$ curves for smaller NPs because it would have occurred at even lower energies, which were not surveyed.

The size of the nanoparticles affects $\delta^i_{nucleus}$ due to the higher self-absorption in larger nanoparticles. This process decreases the amount of energy transferred to the nucleus and the cytoplasm. The value of $\delta^i_{nucleus}$ therefore decreases with the rise of AuNP size, but this decline depends on the distance of AuNPs from the nucleus (see Figure 6). That is, for "near" localizations, the rise of nanoparticle size can reduce $\delta^i_{nucleus}$ up to 25.14%, while for other localizations, this reduction is not significant. It can be concluded that the benefit of having AuNPs close to the nucleus declines as their size increases.

Besides $\delta^i_{nucleus}$, the fraction of deposited energy which went into the nanoparticles δ^i_{np} was also investigated. Values of δ^i_{np} were calculated for the investigated intracellular nanoparticle localizations by inserting simulation outputs into equation (5). The influence of localization on δ^i np is observed only for a few cases, which are presented in Figure 8.

For certain localizations of the nanoparticles, crossfire absorption effect can decrease the amount of the energy deposited in the intended target. It should be noted that even though the macroscopic concentration of nanoparticles in the tissue is the same for all investigated localizations, the microscopic concentration at the cellular level is different. For example, the local concentration of nanoparticles which are distributed in a thin layer at the nuclear envelope is objectively higher than the local concentration of the nanoparticles distributed in the nucleus itself, or in the cell interior. Therefore, in the case of AuNPs attached to the nucleus envelope, the nanoparticles are closer to each other
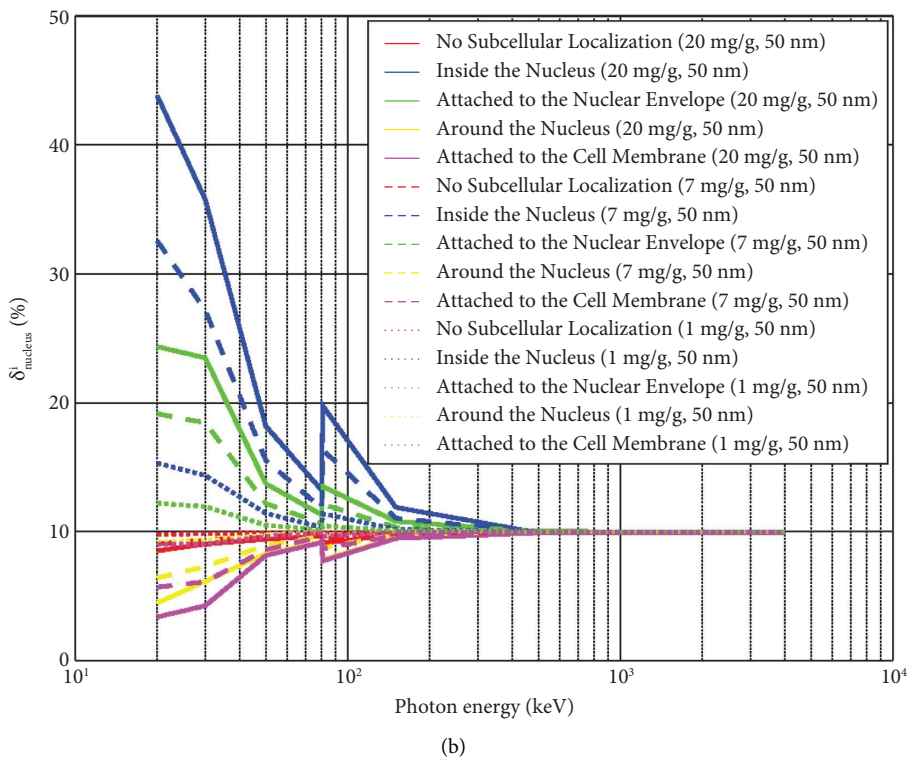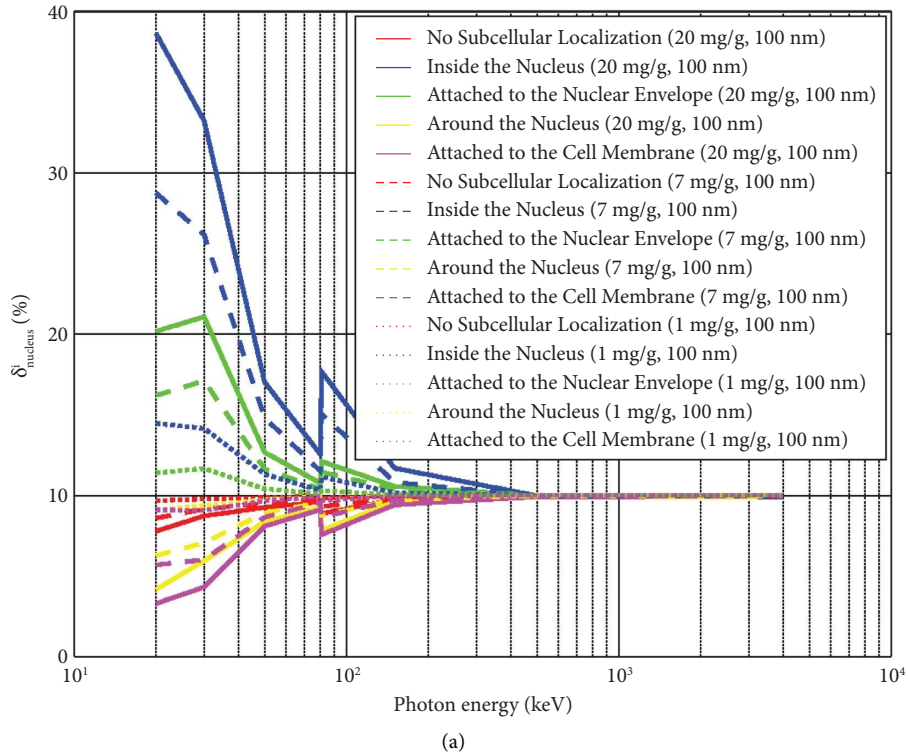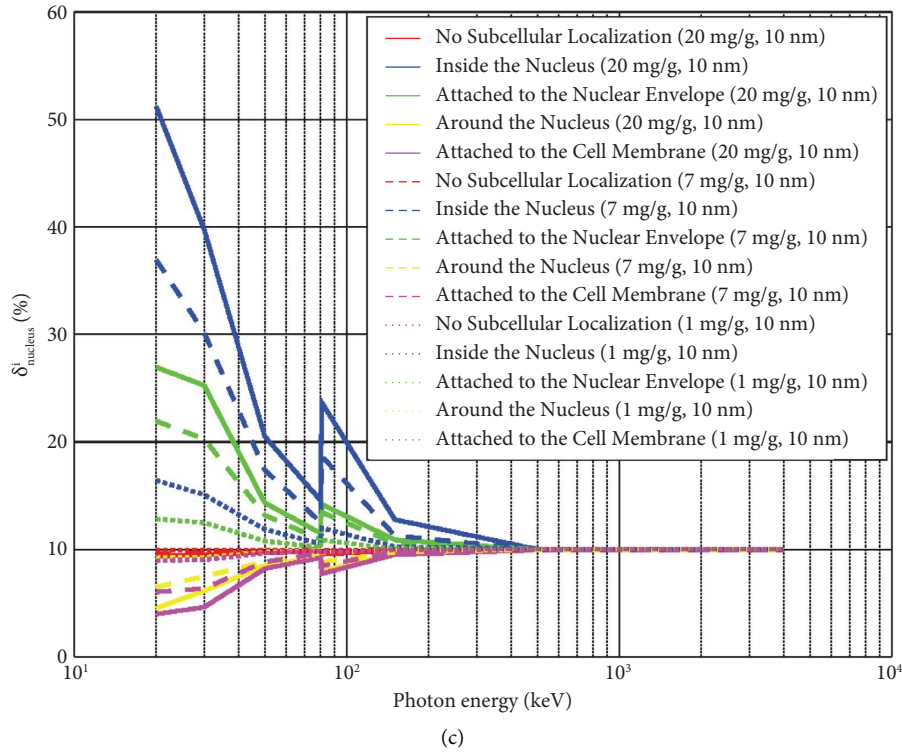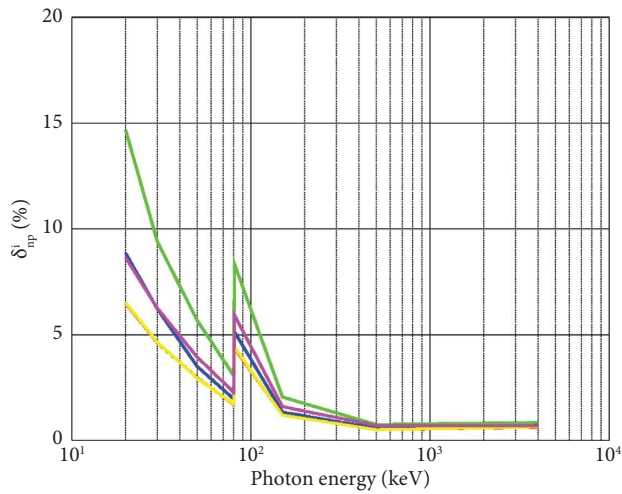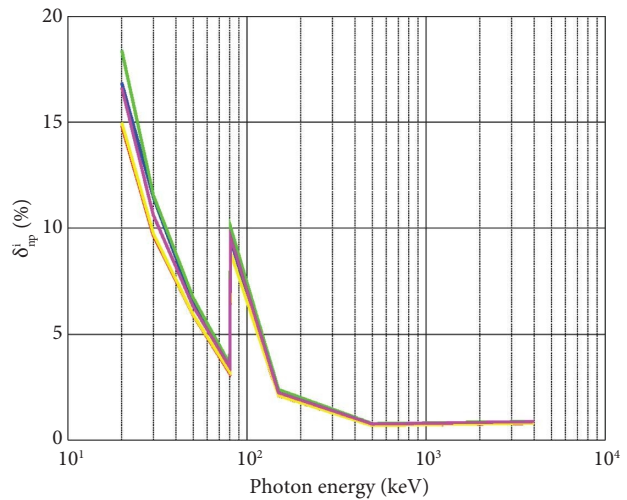
(a)

(b)

FIGURE 7: Continued.

(c)

FIGURE 7: Influence of spherical AuNP intracellular localization. Graphs show the dependence of the fraction of deposited energy delivered to the nucleus $\delta^{i}_{nucleus}$ on the photon beam energy for nanoparticle diameters of (a) 10 nm, (b) 50 nm, and (c) 100 nm. For each nanoparticle size, graphs of various colors pertain to the five different nanoparticle localizations, while different lines of the same color (solid, dashed, and dotted) refer to three nanoparticle concentrations (20, 7, and 1 (mg Au)/(g H_2O), respectively).
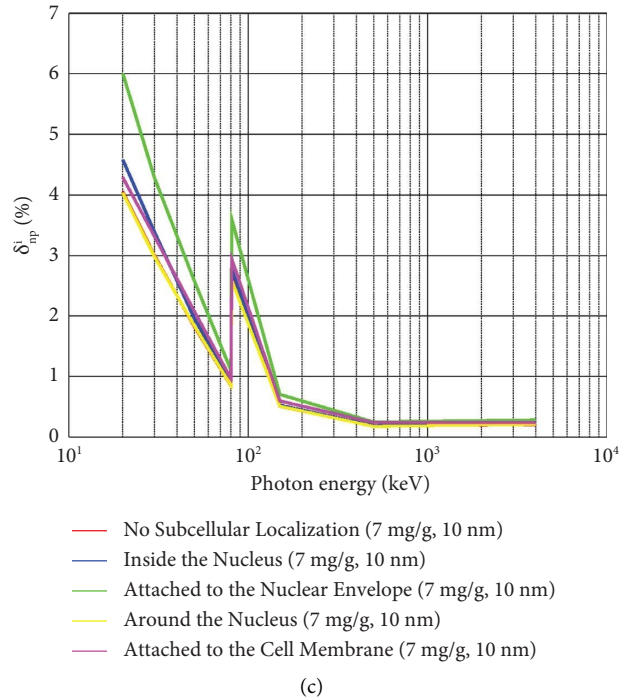

(a)

(b)

FIGURE 8: Continued.

(c)

FIGURE 8: Influence of spherical AuNP intracellular localization. Graphs show the dependence of the fraction of deposited energy that got absorbed in the nanoparticles δ^i_{np} on the photon beam energy when nanoparticle concentration and diameter were, respectively, (a) 20 (mg Au)/(g H_2O) and 10 nm, (b) 20 (mg Au)/(g H_2O) and 50 nm, and (c) 7 (mg Au)/(g H_2O) and 10 nm. Graphs of various colors pertain to the five different nanoparticle localizations.

causing maximum crossfire absorption of the secondary electrons emitted by neighbouring particles. Self-absorption is dominant for the large-radius nanoparticles. However, at lower radii of nanoparticles and at higher concentrations, the influence of crossfire absorption on δ^i_{np} becomes significant. That can be seen in Figure 8, which presents the few most prominent cases for low-volume and high-concentration NPs.

In this study, we investigated five different nanoparticle localizations including two extreme ones: inside the cell nucleus itself, which is the targeted volume, and at the cell membrane, which is as far from the target as possible. In the low-energy region, $\delta^i_{nucleus}$ can differ up to one order of magnitude among nanoparticle localizations. In the high-energy region, $\delta^i_{nucleus}$ is independent of nanoparticle localization and incident photon beam energy, which reveals that for high photon beam energies, the localization of nanoparticles is of no significance. These observations suggest that, for certain irradiation conditions, carefully directed nanoparticle localization could greatly improve the usefulness of deposited radiation energy. Being aware of these facts, future studies which will investigate more realistic cell models should be focused on photon beam energies below 150 keV.

4. Conclusion

This study has investigated the influence that the shape and localization of gold nanoparticles used for enhancing photon radiotherapy have on the energy deposited in the tissue loaded with them. Parameters that have also been varied include the energy of the incident photon beam, nanoparticle size, and concentration. Radiation transport and energy deposition have been simulated using the Geant4 Monte Carlo toolkit, with optimally adjusted model parameters.

Three AuNP shapes have been considered (nanospheres, nanorods, and square nanoplates), for which uniform distribution has been assumed. Regarding the influence of nanoparticle shape, the following has been concluded from simulation results:

(i) Shapes with a higher volume-to-surface ratio and a larger mean straight-line path lead to less radiation energy being deposited in the surrounding medium (water or tissue), at all photon energies and for all AuNP sizes and concentrations. Out of the three investigated shapes, nanoplates would be the most favorable with regard to this usable deposited energy, while nanospheres would be the least beneficial.

(ii) The influence of nanoparticle shape varies with the photon beam energy, being most distinct at low energies (with the usable deposited energy differing up to 19% for the three investigated shapes), subsiding as the energy rises, and becoming absent at highest investigated photon energies.

(iii) As the concentration of AuNPs rises, the importance of their shape becomes more prominent with regard to the usable deposited energy.

(iv) The larger the AuNPs, the greater the difference between the usable energies deposited by nanoparticles of various shapes.

Five different localizations of spherical AuNPs within a cell have been considered: inside the nucleus, attached to the nuclear envelope, around the nucleus, attached to the cell membrane, and with no specific localization (i.e., distributed throughout the cell, including the nucleus). At the cellular level, the usable energy deposited by the therapeutic photon beam has been equated with the energy delivered to the cell nucleus, and various localizations have been compared according to it. The following conclusions have been reached, based on simulation results:

(i) As expected, the energy deposited in the nucleus is highest when AuNPs are inside the nucleus itself. Results for the other four localizations have shown that the farther from the nucleus the nanoparticles are, the lower the fraction of deposited energy that goes into it. The second most efficient distribution of AuNPs is the one at the nuclear envelope, followed by the case of no localization, then by AuNPs distributed around the nucleus, and finally by the nanoparticles adhering to the cell membrane. The greatest difference has been observed between AuNPs localized inside the nucleus and those attached to the cell membrane, with the energy to the nucleus being up to 12.84 times larger in the former case.

(ii) The influence of localization on the energy delivered to the nucleus generally lessens with the increase of photon beam energy, becoming almost irrelevant at beam energies above 150 keV. An exception to this trend is observed for 81 keV photons, since the K-edge energy of gold is at 80.7 keV. For AuNPs inside the nucleus or attached to the nuclear envelope, the fraction of energy delivered to the nucleus generally declines with the increase of photon beam energy. For AuNPs distributed around the nucleus or attached to the cell membrane, the dependence on beam energy is less pronounced and has an opposite trend, with the fraction of energy delivered to the nucleus rising as the photon beam energy increases. In the case of no localization, the fraction of energy delivered to the nucleus is almost independent of the incident beam energy throughout the investigated energy range. For all localizations, a deviation from the described trends appears at the K-edge energy of gold. Also, a slight deviation can be observed at the photon beam energy of 30 keV, in the case when 100 nm AuNPs are attached to the nuclear envelope.

(iii) For AuNPs inside the nucleus or at its envelope, the fraction of the energy delivered to the nucleus declines with the increase in nanoparticle size, due to self-absorption of radiation energy inside the AuNPs themselves. For all other localizations, nanoparticle size has little to no effect on the fraction of energy deposited in the nucleus. As a consequence, the importance of nanoparticle localization, with respect to the energy delivered to the nucleus, lessens as the NPs become larger.

(iv) As the nanoparticle concentration rises, their localization becomes more significant. The fraction of the energy deposited in the nucleus rises with the concentration of nanoparticles for the "near" localizations, while the opposite is observed for "far" localizations.

(v) For localizations with higher packing densities of AuNPs, more of the energy gets self-absorbed, i.e., remains in the nanoparticles themselves. This is especially the case for nanoparticles attached to the nuclear envelope, when multi-layer stacking of NPs occurs. The loss of deposited radiation energy to the NPs is lowest when they are distributed around the nucleus or not localized at all. However, the effect of nanoparticle stacking is only slight in most of the investigated cases.

Seeing that both nanoparticle shape and their localization have been shown to affect the energy deposition efficiency only at photon energies below ~100 keV, future studies of this kind can focus on this energy range alone. This should be able to save much of computer processing time because obtaining simulation results with an acceptable level of confidence at higher photon energies is more demanding of computational resources. Such future investigations may probe various other nanoparticle shapes or localizations, using more realistic cell models. The combined effect of nanoparticle shape and localization can also be analyzed.

The electronic equilibrium implemented in the present paper assumes that the representative volume is surrounded by many other volumes identical to it. For this assumption to be valid, the size of the region encompassing the representative volume, filled by the other identical volumes, would have to be at least as big as the largest range of secondary electrons produced by the photon beam. Furthermore, the whole of that region would have to be exposed to the same photon fluence, i.e., no photon beam attenuation should occur across it. Since deviations from the described conditions affect the exactness of simulation results, an upcoming study by the authors will address these issues in more detail.

It should be noted that the present study is focused on one aspect of the physical stage of photon radiotherapy, namely, on the energy deposition and distribution in connection to nanoparticle shape and localization. The outcome of a radiotherapy treatment, though largely dependent on energy deposition patterns, is further influenced by the chemical and biological phases of radiation effects in living matter. There have already been efforts to perform simulations which encompass these further stages of cells' response to radiation, and more such investigation is yet to be conducted in regard to enhancing radiotherapy with nanoparticles of particular shapes and localizations [43–45].

Results and conclusions provided by the present study can serve as guidelines in the designing phases of gold nanoparticles intended for use in photon radiotherapy. They can point to the steps that are justified and worthwhile while engineering and modifying the properties of AuNPs—their shape and their attachment specificity—so that highest usable dose enhancement is achieved.

Appendix

A. Physical Models of Electron Transport in Geant4 Monte Carlo Simulations

There are two general types of Monte Carlo models for calculating radiation energy deposition in photon radiotherapy at micro- and nanoscales, which differ in the treatment of electron transport: track-structure (TS) and condensed history (CH) models. TS codes simulate each electron interaction down to the energies of several electron volts but require sizeable quantities of input material data and involve time-consuming computations. Track-structure models of electron transport in liquid water and gold have recently been developed by the Geant4-DNA team [46–48]. Version 11.0 of Geant4, which came out in December of 2021, was the first to include the track-structure model for electron transport in gold. While these new models are being tested and verified, available CH algorithms can offer a reliable framework for energy deposition calculations, provided the parameters of the models are set in a suitable manner. The version of Geant4 used for the present study was 10.7, released in December of 2020.

Simulations performed within the current study have utilized the Geant4 Livermore condensed history algorithm of electron transport for calculating energy deposition at nanoscale. To make the results obtained from this algorithm as accurate as possible, the parameters that define it have been set at values that bring it as near as achievable to event-by-event electron tracking. Monte Carlo codes which utilize the CH model usually follow electrons only down to an energy of about 1 keV and also merge (or *condense*) low-energy transfer events into steps, over which the effect that these events have on energy deposition is averaged. The only input data that such codes require for computing energy deposition patterns are the electron stopping powers, which are tabulated with high accuracy for all elements and easily calculated for any material. CH codes are much less demanding of computational resources than TS codes and more easily adapted to new applications. The main shortcoming of the CH codes is their low spatial resolution, which is at around 0.1 mm, while TS codes can reach sub-nanometer resolution [49]. To overcome this, some CH codes apply a "mixed" approach, grouping low-energy transfer collisions into steps, while simulating high-energy transfer collisions (also called "hard" collisions) discretely, based on single-scattering cross sections. Setting the hard collision energy transfer threshold at a particularly low value should, in principle, allow a mixed CH code to simulate all collisions in a discrete way, thus approximating a TS code [31, 32].

The Livermore model, available in Geant4 through the G4EmLivermorePhysics constructor, supplemented by other constructors dedicated to relaxation processes (including fluorescent photon and Auger electron emissions), incorporates all relevant aspects of electron transport [32, 33, 50, 51]. The photons and electrons that originate from electron interactions are further followed in the same detailed way as the incident photons and the electrons that they produce. Parameters of the model that were varied in order to bring it closest to a TS algorithm included the *production cut* (i.e., the energy limit for a secondary electron at the instance of creation below which it is not propagated, but rather has its energy deposited locally, at the site of creation), the *step-size limit for electrons* (i.e., the maximum deterministically assigned step size), and the *lowest electron energy* (below which the propagation of an electron is terminated and its energy deposited locally). Simulations for the current study were at first run with these three adjustable parameters set at particularly low values: production cut was set at 10 eV, step-size limit at 0.1 nm, and lowest electron energy at 1 eV. However, with all three parameters adopted so stringently, computation times were excessively long. An optimal set of the three parameters was then searched for by changing one at a time, with the other two unaltered. An additional criterion for accepting a particular value for a parameter, besides the duration of a simulation run, was the quality of the obtained simulation results: a result was considered acceptable if it deviated by less than 1% from the one obtained with the same number of photon histories when all three adjustable parameters were at their lowest values. An extensive survey of simulation times and of the associated result quality for various nanoparticle concentrations and sizes revealed that the Livermore model was very sensitive to changes in the production cut and lowest electron energy, in agreement with conclusions reached elsewhere [50]. These two parameters were therefore kept at the initial stringent values of 10 eV and 1 eV, respectively. Variation of the step-size limit, on the other hand, barely affected the results. This third parameter was therefore eventually set at the maximum value available in Geant4, which is *DBL_MAX*, with no noticeable influence on result variability or uncertainty. Such a relaxation of the step-size limit made the computations approximately 100 times faster compared to those utilizing the initial step size of 0.1 nm.

Data Availability

Additional data (simulation results) that support the findings of this study are available through one of the authors, Slobodan Milutinović, who can be reached at slobodan.milutinovicm@gmail.com.

Conflicts of Interest

The authors declare that they have no conflicts of interest.

Acknowledgments

References

[1] R. A. Freitas, *Nanomedicine, Volume I: Basic Capabilities*, CRC Press, Austin, TX, USA, 1st edition, 1999.

[2] S. K. Murthy, "Nanoparticles in modern medicine: state of the art and future challenges," *International Journal of Nanomedicine*, vol. 2, pp. 129–141, 2007.

[3] J. Wolfram, M. Zhu, Y. Yang et al., "Safety of nanoparticles in medicine," *CDT*, vol. 16, no. 14, pp. 1671–1681, 2015.

[4] A. M. Grumezescu and A. Ficai, Eds., *Nanostructures for Cancer Therapy*, Elsevier, Amsterdam, Netherlands, 1st edition, 2017.

[5] I. Tremi, E. Spyratou, M. Souli et al., "Requirements for designing an effective metallic nanoparticle (NP)-Boosted radiation therapy (RT)," *Cancers*, vol. 13, p. 3185, 2021.

[6] S. D. Steichen, M. Caldorera-Moore, and N. A. Peppas, "A review of current nanoparticle and targeting moieties for the delivery of cancer therapeutics," *European Journal of Pharmaceutical Sciences*, vol. 48, no. 3, pp. 416–427, 2013.

[7] P. Talarska, M. Boruczkowski, and J. Żurawski, "Current knowledge of silver and gold nanoparticles in laboratory research—application, toxicity, cellular uptake," *Nanomaterials*, vol. 11, no. 9, p. 2454, 2021.

[8] I. Hammami, N. M. Alabdallah, A. A. jomaa, and M. kamoun, "Gold nanoparticles: synthesis properties and applications," *Journal of King Saud University Science*, vol. 33, no. 7, Article ID 101560, 2021.

[9] E. Lechtman, N. Chattopadhyay, Z. Cai, S. Mashouf, R. Reilly, and J. P. Pignol, "Implications on clinical scenario of gold nanoparticle radiosensitization in regards to photon energy, nanoparticle size, concentration and location," *Physics in Medicine and Biology*, vol. 56, no. 15, pp. 4631–4647, 2011.

[10] B. Koger and C. Kirkby, "A method for converting dose-to-medium to dose-to-tissue in Monte Carlo studies of gold nanoparticle-enhanced radiotherapy," *Physics in Medicine and Biology*, vol. 61, no. 5, pp. 2014–2024, 2016.

[11] C. Kirkby, B. Koger, N. Suchowerska, and D. R. McKenzie, "Dosimetric consequences of gold nanoparticle clustering during photon irradiation," *Medical Physics*, vol. 44, no. 12, pp. 6560–6569, 2017.

[12] S. H. Cho, "Estimation of tumour dose enhancement due to gold nanoparticles during typical radiation treatments: a preliminary Monte Carlo study," *Physics in Medicine and Biology*, vol. 50, no. 15, pp. N163–N173, 2005.

[13] E. Amato, A. Italiano, and S. Pergolizzi, "Gold nanoparticles as a sensitising agent in external beam radiotherapy and brachytherapy: a feasibility study through Monte Carlo simulation," *IJNT*, vol. 10, no. 12, p. 1045, 2013.

[14] S. Asadi, M. Vaez-zadeh, S. F. Masoudi, F. Rahmani, C. Knaup, and A. S. Meigooni, "Gold nanoparticle-based brachytherapy enhancement in choroidal melanoma using a full Monte Carlo model of the human eye," *Journal of Applied Clinical Medical Physics*, vol. 16, no. 5, pp. 344–357, 2015.

[15] Y. Lin, H. Paganetti, S. J. McMahon, and J. Schuemann, "Gold nanoparticle induced vasculature damage in radiotherapy: comparing protons, megavoltage photons, and kilovoltage photons," *Medical Physics*, vol. 42, no. 10, pp. 5890–5902, 2015.

[16] M. P. Martinov and R. M. Thomson, "Heterogeneous multiscale Monte Carlo simulations for gold nanoparticle radiosensitization," *Medical Physics*, vol. 44, no. 2, pp. 644–653, 2017.

[17] W. Sung, S.-J. Ye, A. L. McNamara et al., "Dependence of gold nanoparticle radiosensitization on cell geometry," *Nanoscale*, vol. 9, no. 18, pp. 5843–5853, 2017.

[18] M. Laprise-Pelletier, Y. Ma, J. Lagueux, M. F. Côté, L. Beaulieu, and M. A. Fortin, "Intratumoral injection of low-energy photon- emitting gold nanoparticles: a micro-dosimetric Monte Carlo-based model," *ACS Nano*, vol. 12, no. 3, pp. 2482–2497, 2018.

[19] W. B. Li, A. Belchior, M. Beuve et al., "Intercomparison of dose enhancement ratio and secondary electron spectra for gold nanoparticles irradiated by X-rays calculated using multiple Monte Carlo simulation codes," *Physica Medica*, vol. 69, pp. 147–163, 2020.

[20] E. Engels, S. Bakr, D. Bolst et al., "Advances in modelling gold nanoparticle radiosensitization using new Geant4-DNA physics models," *Physics in Medicine and Biology*, vol. 65, no. 22, Article ID 225017, 2020.

[21] F. Poignant, C. Monini, É. Testa, and M. Beuve, "Influence of gold nanoparticles embedded in water on nanodosimetry for keV photon irradiation," *Medical Physics*, vol. 48, no. 4, pp. 1874–1883, 2021.

[22] Z. Cai, J.-P. Pignol, N. Chattopadhyay, Y. L. Kwon, E. Lechtman, and R. M. Reilly, "Investigation of the effects of cell model and subcellular location of gold nanoparticles on nuclear dose enhancement factors using Monte Carlo simulation," *Medical Physics*, vol. 40, no. 11, Article ID 114101, 2013.

[23] E. Lechtman and J. P. Pignol, "Interplay between the gold nanoparticle sub-cellular localization, size, and the photon energy for radiosensitization," *Scientific Reports*, vol. 7, no. 1, Article ID 13268, 2017.

[24] F. S. Rasouli and S. F. Masoudi, "Monte Carlo investigation of the effect of gold nanoparticles' distribution on cellular dose enhancement," *Radiation Physics and Chemistry*, vol. 158, pp. 6–12, 2019.

[25] F. S. Rasouli, S. F. Masoudi, and S. Asadi, "On the importance of modeling gold nanoparticles distribution in dose-enhanced radiotherapy&lt," *International Journal of Nanomedicine*, vol. 14, pp. 5865–5874, 2019.

[26] A. Konefał, W. Lniak, J. Rostocka et al., "Influence of a shape of gold nanoparticles on the dose enhancement in the wide range of gold mass concentration for high-energy X-ray beams from a medical linac," *Reports of Practical Oncology and Radiotherapy*, vol. 25, no. 4, pp. 579–585, 2020.

[27] F. Abolaban and E. Taha, "A Monte Carlo study on the effect of nanoparticle shapes on dose enhancement and distribution using 197Au and 195Pt," *Journal of Radiation Research and Applied Sciences*, vol. 13, pp. 698–703, 2020.

[28] S. Agostinelli, J. Allison, K. Amako et al., "Geant4—a simulation toolkit," *Nuclear Instruments and Methods in Physics Research Section A: Accelerators, Spectrometers, Detectors and Associated Equipment*, vol. 506, no. 3, pp. 250–303, 2003.

[29] J. Allison, K. Amako, J. Apostolakis et al., "Geant4 developments and applications," *IEEE Transactions on Nuclear Science*, vol. 53, no. 1, pp. 270–278, 2006.

[30] Advanced Micro Devices, "Amd ryzentm threadrippertm 1950x processor," 2018, https://www.amd.com/en/product/2066.

[31] S. Milutinović and M. Vujisić, "Simulation-based correction of dose enhancement factor values in photon brachytherapy with metal nanoparticle targeting," *Nuclear Science and Techniques*, vol. 31, no. 11, p. 114, 2020.

[32] I. Kyriakou, D. Emfietzoglou, V. Ivanchenko et al., "Microdosimetry of electrons in liquid water using the low-energy models of Geant4," *Journal of Applied Physics*, vol. 122, no. 2, Article ID 024303, 2017.

[33] P. Lazarakis, S. Incerti, V. Ivanchenko et al., "Investigation of track structure and condensed history physics models for applications in radiation dosimetry on a micro and nano scale in Geant4," *Biomed Phys Eng Express*, vol. 4, no. 2, Article ID 024001, 2018.

[34] F. Moradi, K. Rezaee Ebrahim Saraee, S. F. Abdul Sani, and D. Bradley, "Metallic nanoparticle radiosensitization: the role of Monte Carlo simulations towards progress," *Radiation Physics and Chemistry*, vol. 180, Article ID 109294, 2021.

[35] M. Schürmann, J. Scholze, P. Müller, J. Guck, and C. J. Chan, "Cell nuclei have lower refractive index and mass density than cytoplasm," *Journal of Biophotonics*, vol. 9, no. 10, pp. 1068–1076, 2016.

[36] K. Kim and J. Guck, "The relative densities of cytoplasm and nuclear compartments are robust against strong perturbation," *Biophysical Journal*, vol. 119, no. 10, pp. 1946–1957, 2020.

[37] F. Hutchinson, "The molecular basis for radiation effects on cells," *Cancer Research*, vol. 26, no. 9, pp. 2045–2052, 1966.

[38] L. Pan, J. Liu, and J. Shi, "Cancer cell nucleus-targeting nanocomposites for advanced tumor therapeutics," *Chemical Society Reviews*, vol. 47, no. 18, pp. 6930–6946, 2018.

[39] M. Deserno, "How to generate equidistributed points on the surface of a sphere," 2004, https://www.cmu.edu/biolphys/deserno/pdf/sphere_equi.pdf.

[40] J. M. Fernández-Varea, X. Llovet, and F. Salvat, "Cross sections for electron interactions in condensed matter," *Surface and Interface Analysis*, vol. 37, no. 11, pp. 824–832, 2005.

[41] H. T. Nguyen-Truong, "Penn algorithm including damping for calculating the electron inelastic mean free path," *Journal of Physical Chemistry C*, vol. 119, no. 14, pp. 7883–7887, 2015.

[42] F. Poignant, A. Ipatov, O. Chakchir et al., "Theoretical derivation and benchmarking of cross sections for low-energy electron transport in gold," *European Physical Journal E: Soft Matter*, vol. 135, no. 4, p. 358, 2020.

[43] W. Friedland, M. Dingfelder, P. Kundrát, and P. Jacob, "Track structures, DNA targets and radiation effects in the biophysical Monte Carlo simulation code PARTRAC," *Mutation Research: Fundamental and Molecular Mechanisms of Mutagenesis*, vol. 711, no. 1-2, pp. 28–40, 2011.

[44] W. Friedland, E. Schmitt, P. Kundrát et al., "Comprehensive track-structure based evaluation of DNA damage by light ions from radiotherapy-relevant energies down to stopping," *Scientific Reports*, vol. 7, no. 1, Article ID 45161, 2017.

[45] Y. Matsuya, T. Kai, Y. Yoshii et al., "Modeling of yield estimation for DNA strand breaks based on Monte Carlo simulations of electron track structure in liquid water," *Journal of Applied Physics*, vol. 126, no. 12, Article ID 124701, 2019.

[46] D. Sakata, I. Kyriakou, S. Okada et al., "Geant4-DNA track-structure simulations for gold nanoparticles: the importance of electron discrete models in nanometer volumes," *Medical Physics*, vol. 45, no. 5, pp. 2230–2242, 2018.

[47] D. Sakata, I. Kyriakou, H. N. Tran et al., "Electron track structure simulations in a gold nanoparticle using Geant4-DNA," *Physica Medica*, vol. 63, pp. 98–104, 2019.

[48] S. Incerti, I. Kyriakou, M. A. Bernal et al., "Geant4-DNA example applications for track structure simulations in liquid water: a report from the Geant4-DNA Project," *Medical Physics*, vol. 45, no. 8, pp. e722–e739, 2018.

[49] M. Dingfelder, "Track-structure simulations for charged particles," *Health Physics*, vol. 103, no. 5, pp. 590–595, 2012.

[50] I. Kyriakou, V. Ivanchenko, D. Sakata et al., "Influence of track structure and condensed history physics models of Geant4 to nanoscale electron transport in liquid water," *Physica Medica*, vol. 58, pp. 149–154, 2019.

[51] S. Incerti, B. Suerfu, J. Xu et al., "Simulation of Auger electron emission from nanometer-size gold targets using the Geant4 Monte Carlo simulation toolkit," *Nuclear Instruments and Methods in Physics Research Section B: Beam Interactions with Materials and Atoms*, vol. 372, pp. 91–101, 2016.